CONDENSED MATTER PHYSICS

Giant coercivity and enhanced intrinsic anomalous Hall effect at vanishing magnetization in a compensated kagome ferrimagnet

Jonathan M. DeStefano[1], Elliott Rosenberg[1], Guodong Ren[2], Yongbin Lee[3], Zhenhua Ning[3], Olivia Peek[1], Kamal Harrison[1,4,5], Saiful I. Khondaker[4,5,6], Liqin Ke[3,7], Igor I. Mazin[8], Juan Carlos Idrobo[2,9], Jiun-Haw Chu[1]*

Ferrimagnets that can be driven to magnetic compensation show promise for use in spintronics as they exhibit a finite anomalous Hall effect at zero magnetic field without having a substantial magnetic moment. Compensated ferrimagnet spintronic devices with both a large anomalous Hall effect and a high coercivity would be simultaneously easy to read and difficult to erase. The kagome ferrimagnet $TbMn_6Sn_6$ has been reported to host a large intrinsic anomalous Hall effect. Here, we demonstrate that doping the Mn sites with Cr drives the system toward magnetic compensation. For nearly compensated compositions at low temperatures, giant coercive fields exceeding 14 T are observed. Additionally, Cr doping markedly enhances the intrinsic anomalous Hall effect, which can be attributed to a shift in the Fermi level. Our results extend the range of unique magnetic states observed in kagome materials, demonstrating that chemical doping is an effective strategy to tune and realize these states.

INTRODUCTION

Compensated ferrimagnets have recently emerged as a promising material platform for spintronics applications, combining advantageous properties of both ferromagnets and antiferromagnets (*1*–*3*). In antiferromagnets, the net moment is zero by symmetry. This feature leads not only to faster switching times, reduced stray fields, and resistance against external fields but also to difficulty to read and write magnetic domains. A related class of Luttinger-compensated ferrimagnets (*4*) also features exact compensation, albeit not by symmetry but by virtue of Luttinger theorem.

These can be insulators, or half-metals (metallic in one spin channel). A more promising possibility is chemically compensated ferrimagnets, which are metallic in both spin channels. There, the net magnetization can be tuned to zero by controlling the chemical composition of their inequivalent spin sublattices. A great advantage here is that the net magnetic moment can be tunable by chemical composition or temperature so that it is small, but not zero, thus allowing domain control by external fields. Another important advantage is that despite near-zero magnetization, compensated ferrimagnets allow for large (on the order of hundreds meV) exchange splitting. Consequently, they can exhibit finite anomalous Hall effect (AHE), providing a relatively straightforward reading mechanism.

A well-known class of compensated ferrimagnets is the rare-earth transition-metal alloys (*5*). In these materials, the magnetic moments of rare-earth and transition-metal ions are antiferromagnetically coupled, and the net magnetic moment can be controlled by tuning their relative concentrations. The magnetization of the rare-earth and transition-metal moments has different temperature dependencies. As a result, zero net magnetization occurs at a compensation temperature, denoted as T^*, which can be smoothly modulated by chemical composition. While amorphous materials have dominated the study of rare-earth transition-metal compensated ferrimagnets, crystalline compounds have received comparatively less attention. Unlike amorphous materials, crystalline materials host well-defined Bloch energy bands, characterized by Berry curvatures capable of generating large intrinsic AHEs. Consequently, the search and design of materials with large Berry curvature has also emerged as a key focal point in spintronics research (*6*).

Here, we report the realization of compensated ferrimagnetism in a rare-earth transition-metal intermetallic compound, $Tb(Mn_{1-x}Cr_x)_6Sn_6$. $Tb(Mn_{1-x}Cr_x)_6Sn_6$ belongs to the RT_6X_6 (R = rare earth, T = transition metal, X = Si, Ge, Sn) family, known for its kagome lattice structure and intriguing band structure features such as flat bands, van Hove singularities, and Dirac points (*7*–*9*). Notably, the ferrimagnet $TbMn_6Sn_6$ exhibits a large intrinsic AHE, which was initially attributed to Berry curvature arising from a gapped two-dimensional (2D) Dirac point above but near the Fermi level (*10*). This picture, if correct, would preclude Cr doping (hole doping) as a knob to tune the net magnetization without decreasing the intrinsic AHE, since that would shift the Fermi level away from the Dirac point. Furthermore, the 2D nature of the Dirac point would limit the large AHE to one particular geometry. Fortunately, it was later shown (*11*–*13*) that the AHE is accumulated over the entire Brillouin zone (BZ) and does not depend dramatically on the Fermi level; it was also shown that the AHE in similar compounds is 3D (*14*), which is also favorable for applications.

Here, we show that the substitution of Cr for Mn reduces the magnetic moment of the transition-metal site, which eventually turns $Tb(Mn_{1-x}Cr_x)_6Sn_6$ into a compensated ferrimagnet. Near compensation, we observed a divergence of the coercive field at low temperatures. Furthermore, contrary to the initially advocated 2D Dirac point scenario, Cr substitution substantially enhances intrinsic AHE, likely due to the tuning of the Fermi level to various Berry

[1]Department of Physics, University of Washington, Seattle, WA 98112, USA. [2]Materials Sciences & Engineering Department, University of Washington, Seattle, WA 98115, USA. [3]Ames Laboratory, U.S. Department of Energy, Ames, IA 50011, USA. [4]Department of Physics, University of Central Florida, Orlando, FL 32816, USA. [5]NanoScience Technology Center, University of Central Florida, Orlando, FL 32826, USA. [6]School of Electrical Engineering and Computer Science, University of Central Florida, Orlando, FL 32826, USA. [7]Department of Materials Science and Engineering, University of Virginia, Charlottesville, VA 22904, USA. [8]Department of Physics and Astronomy and Quantum Science and Engineering Center, George Mason University, Fairfax, VA 22030, USA. [9]Physical and Computational Sciences Directorate, Pacific Northwest National Laboratory, Richland, WA 99354, USA.
*Corresponding author. Email: jhchu@uw.edu

curvature hotspots (*13*). Our findings pave the way for the rational design of a compensated ferrimagnet with a large intrinsic AHE.

RESULTS

Basic characterization

High-quality single crystals of $Tb(Mn_{1-x}Cr_x)_6Sn_6$ with x up to 0.55 were grown using a Sn flux method. The magnetization and magneto-transport properties of these crystals were measured by the vibration sample magnetometry (VSM) option of a Quantum Design Physical Property Measurement System (PPMS) Dynacool and standard AC electrical transport techniques, respectively. Further details can be found in Materials and Methods. Figure 1A shows the crystal structure of $TbMn_6Sn_6$, which consists of two layers of kagome lattices formed by Mn atoms and one layer of triangular lattice composed of Tb atoms, viewed along the *ab* plane (top) and *c* axis (bottom). This crystal structure is preserved with Cr doping, as exemplified in the *Z*-contrast atomic-resolution scanning transmission electron microscope (STEM) image shown in Fig. 1B where the *ab*-plane kagome motif can be observed in an $x = 0.55$ sample. Additionally, atomic-resolution electron energy-loss spectroscopy (EELS) was used to map out the elemental distribution in this sample, which is presented in Fig. 1C. Notably, the Cr substitution for Mn is relatively homogeneous even at the nanometer scale.

$TbMn_6Sn_6$ orders ferrimagnetically at 423 K (T_c) (*15*). Within the layers, the Mn moments and the Tb moments order ferromagnetically, but the Tb and Mn layers couple antiferromagnetically, resulting in a ferrimagnetic structure where Tb and Mn moments are antiparallel [schematically shown in the top portion of Fig. 2A (FiM IP)]. Neutron scattering studies on polycrystalline samples have revealed that at base temperature the size of Mn moment is 2.4 bohr magnetons (μ_B) and the size of Tb moment is 8.6 μ_B, leading to a net 5.8 μ_B per formula unit along the direction Mn moments (*15*). It should be noted that the saturated magnetization of single crystals of $TbMn_6Sn_6$ from bulk magnetization measurements (*10*, *13*, *16*) is ≈4 μ_B per formula unit (F.U.), which is consistent with our results but less than the value extracted from neutron scattering; this discrepancy has previously been noticed (*16*) and may be due to inherent differences between polycrystalline and single-crystal samples. Figure 2B shows the temperature dependence of the magnetization of $Tb(Mn_{1-x}Cr_x)_6Sn_6$ with a small in-plane (top) and out-of-plane (bottom) magnetic field of 0.1 T. The ferrimagnetic ordering temperature of the $x = 0$ sample exceeds the instrument limit (400 K); thus, it is not visible within this dataset. Nevertheless, a sudden decrease in in-plane magnetization and an increase in out-of-plane magnetization are observed at 309 K (T_{sr}). The abrupt change in magnetization is associated with a spin reorientation transition (*10*), where the Tb and Mn moments switch from a high-temperature in-plane orientation to a low-temperature out-of-plane orientation (FiM OOP), as shown in the bottom portion of Fig. 2A. This transition can be attributed to the competition between the *c*-axis uniaxial anisotropy favored by the Tb moments and the easy-plane anisotropy preferred by the Mn moments. At high temperatures, the Tb moments fluctuate more due to a weaker exchange interaction, allowing the easy-plane anisotropy of the Mn moments to dominate. At low temperatures, the scenario is reversed, and the *c*-axis uniaxial anisotropy of the Tb moments prevails (*13*, *17*).

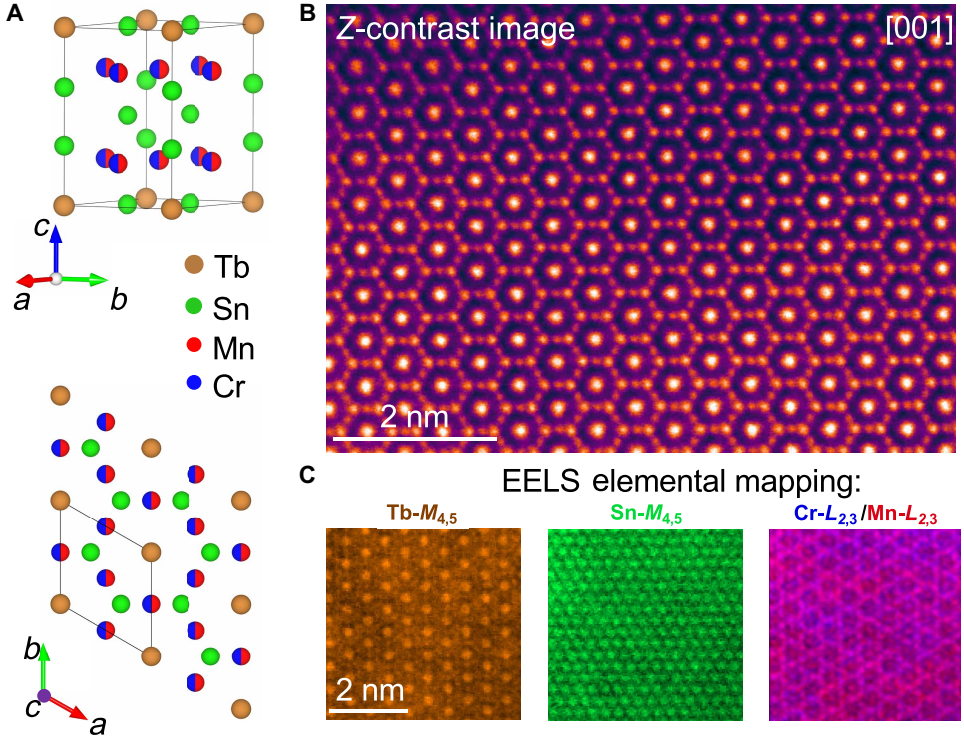

Fig. 1. Atomic-scale visualization of $Tb(Mn_{1-x}Cr_x)_6Sn_6$ kagome lattice. (**A**) Atomic models of the $Tb(Mn_{1-x}Cr_x)_6Sn_6$ lattice viewed along the *ab* plane in the top panel and along the *c* axis in the bottom panel. The kagome layers have a mixed occupancy of Cr dopants and Mn (depicted in blue and red, respectively). (**B**) *Z*-contrast atomic-resolution STEM image of an $x = 0.55$ crystal viewed along the *c* axis. (**C**) Color maps of elemental distribution by atomic-resolution EELS. Left, Tb ($M_{4,5}$ edge); middle, Sn ($M_{4,5}$ edge); right, mixed distribution of Cr and Mn ($L_{2,3}$ edges).

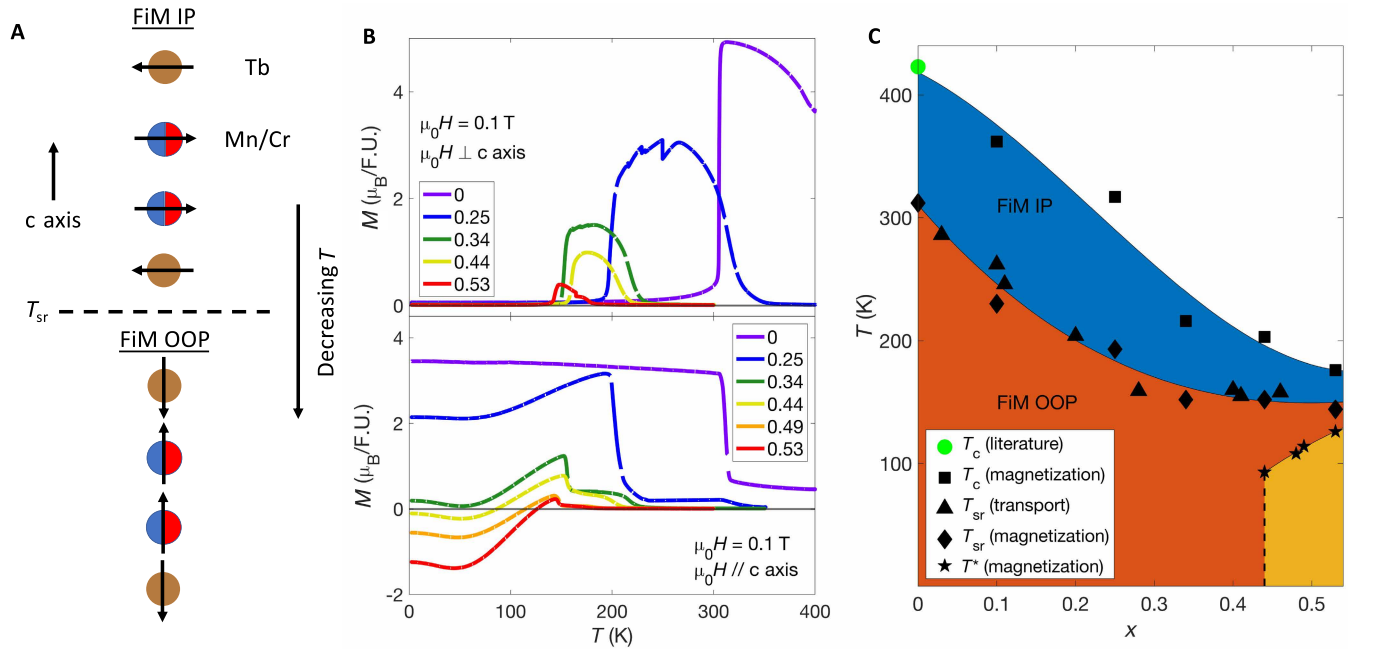

Fig. 2. Spin reorientation transition and the phase diagram of $Tb(Mn_{1-x}Cr_x)_6Sn_6$. (**A**) Orientation of magnetic moments of $Tb(Mn_{1-x}Cr_x)_6Sn_6$ in the high-temperature ferrimagnetic in-plane (FiM IP) (top) and low-temperature ferrimagnetic out-of-plane (FiM OOP) (bottom) phases. (**B**) Low-field magnetization as a function of temperature of $Tb(Mn_{1-x}Cr_x)_6Sn_6$ for a variety of x with an in-plane (top) or out-of-plane (bottom) magnetic field of 0.1 T applied. The sudden decrease/increase of in-plane/out-of-plane magnetization indicates the spin reorientation transition at T_{sr}. F.U., formula unit. (**C**) x-T phase diagram of $Tb(Mn_{1-x}Cr_x)_6Sn_6$ as determined from magnetization and transport measurements.

As shown in Fig. 2B, the temperature dependence of the in-plane magnetization for Cr-doped samples closely resemble that of the parent compound except that T_c, T_{sr}, and the magnitude of the magnetization steadily decrease with increasing x. This is consistent with a previous study on polycrystalline samples, where Cr doping reduced the average moment size of the transition metal, thereby suppressing the overall ferrimagnetic ordering temperature (*18*). However, the out-of-plane magnetization exhibits a more intriguing behavior. While the features at T_c and T_{sr} are consistent with the in-plane magnetization data, the out-of-plane magnetization demonstrates a strong temperature dependence below T_{sr}, contrasting with the nearly constant magnetization observed in the parent $TbMn_6Sn_6$ over this temperature range. For the Cr-doped samples, the out-of-plane magnetization decreases with temperature, reaching a local minimum near 60 K. For x greater than 0.4, the magnetization continues to decrease even after reaching zero at T^*, resulting in negative value for temperatures below T^*. This anti-alignment of the moment with the external magnetic field has been observed in other ferrimagnets driven to magnetic compensation by changing temperature (*19*).

Using the magnetization data presented here and the resistivity data presented in note S1, along with the literature value of T_c for $x = 0$ (*15*, *16*), an x-T phase diagram was constructed and is shown in Fig. 2C. It can be seen that both T_c and T_{sr} decrease rapidly with increasing x in the low x regime, but become relatively constant with further doping above approximately $x = 0.3$. For higher Cr concentration, T^* emerges, delineating the boundary of a region where the magnetization is anti-aligned with the external field during the cool-down process. In the following sections, we will examine the hysteresis loop of both the magnetization and the anomalous Hall resistivity as a function of doping and temperature. Our results reveal that this unusual behavior arises from magnetic compensation driven by Cr doping and thermal fluctuations of Tb moments.

Chemical doping–induced magnetic compensation and giant coercivity

We begin by examining the doping dependence at the base temperature. Figure 3A shows the magnetization (top row) and ρ_{xy} (bottom row) as functions of the magnetic field parallel to the c axis at 2.5 K for five representative Cr concentrations. The magnetization of $Tb(Mn_{1-x}Cr_x)_6Sn_6$ shows a clear hysteresis loop characteristic of a hard ferrimagnet with uniaxial anisotropy. As the Cr concentration increases, the saturated magnetization decreases, reaching a value near zero at a composition $x^* \approx 0.43$, before increasing again for $x > x^*$. The reduction in saturated magnetization is accompanied by a considerable increase in the coercive field. A previous neutron scattering study on low-x $Tb(Mn_{1-x}Cr_x)_6Sn_6$ revealed that Cr doping at the Mn site reduces the moment on that site without substantially changing the moment on the Tb site (*18*). Extending this observation to higher dopings suggests that at x^* the total magnetization from the Mn/Cr and Tb moments becomes equal, resulting in a net magnetization of zero. As x increases beyond x^*, the total magnetization of the Tb moments surpasses that of the Mn/Cr moments, causing the net magnetization to rise again, aligning with the Tb moment.

To confirm this hypothesis, we plot M' in the top panel of Fig. 3B, where $M' = M$ for $x < x^*$ and $M' = M$ for $x > x^*$. Here, M represents the experimentally measured zero field magnetization after the application of a large positive field to polarize the moments. The assumption is that M' corresponds to the net magnetization of the Mn/Cr moments minus the net magnetization of the Tb moments.

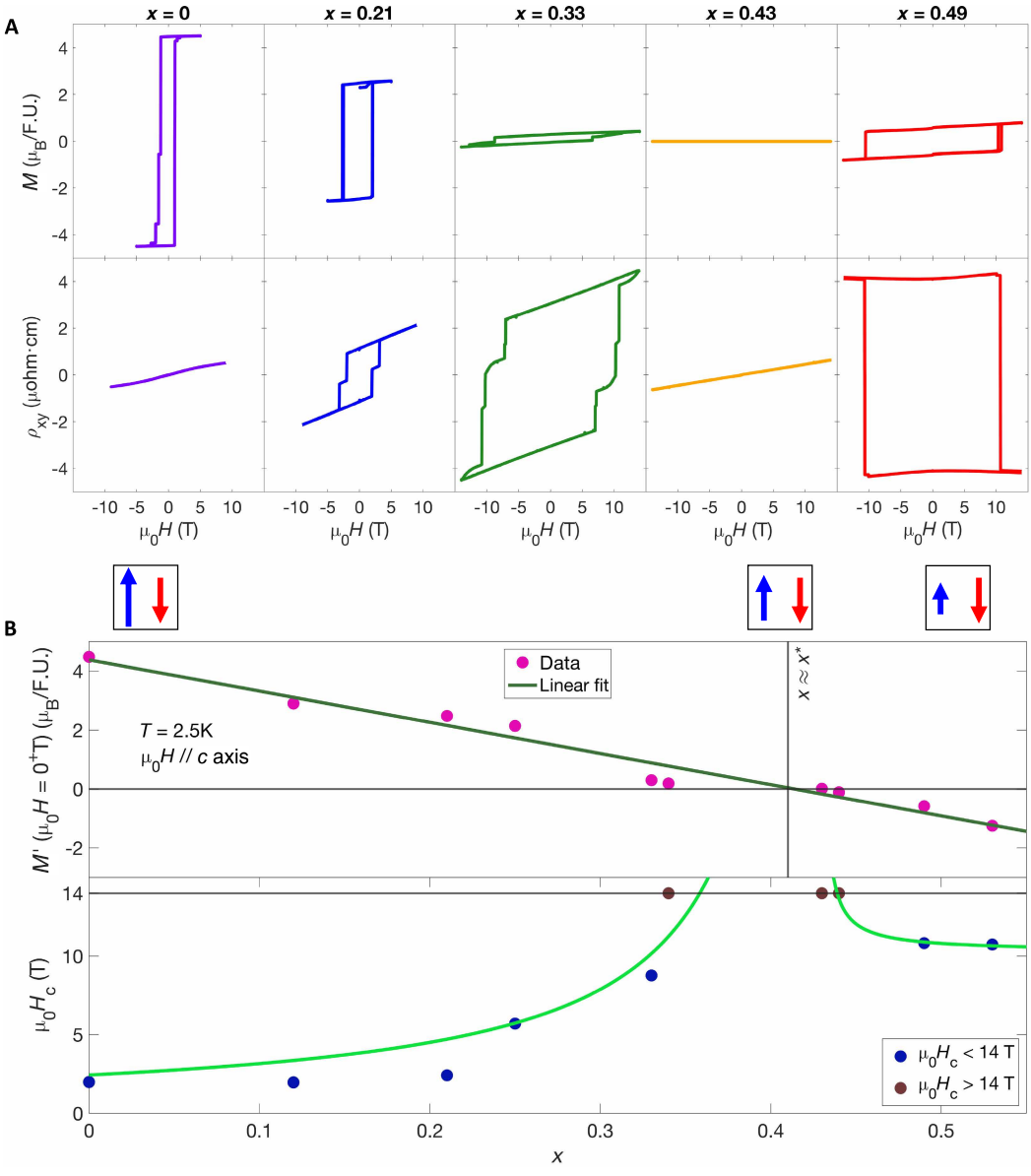

Fig. 3. Magnetic compensation and giant coercivity through chemical doping. (**A**) Magnetization (top row) and ρ_{xy} (bottom row) as a function of magnetic field for a variety of x at 2.5 K. Plots in the same column are from the same x, which is indicated by the text on top of the column. (**B**) Top: M' (described in the main text) as a function of x at 2.5 K with decreasing magnetic field. Bottom: $\mu_0 H_c$ as a function of x from magnetization measurements.

M' decreases roughly linearly as a function of x while (by construction) crossing zero at x^*. A linear fit of these data indicates that the average moment decreases by roughly 1.8 μ_B per Cr substitution, in good agreement with the previous neutron scattering study (*18*). Since each Mn ion has a moment of 2.4 μ_B in $TbMn_6Sn_6$, this implies that each Cr ion in $Tb(Mn_{1-x}Cr_x)_6Sn_6$ carries a moment of 0.6 μ_B if the Mn moments remain the same regardless of doping. This is quite similar to the value of 0.48 μ_B, which was found to be the moment per Cr ion in $TbCr_6Ge_6$ via neutron scattering measurements (*20*). Thus, Cr is likely in a low-spin state in these materials.

To gain further insight, we performed density functional theory (DFT) calculations to investigate the magnetic state of $Tb(Mn_{1-x}Cr_x)_6Sn_6$. We found that for $TbCr_2Mn_4Sn_6$ (with both DFT + U frozen core Tb^{3+}), the lowest energy states correspond to Cr forming 1D in-plane antiferromagnetic chains. Thus, a potential major contribution to the magnetic moment reduction with Cr doping is due neither to dilution of the Mn sublattice by nonmagnetic ions nor to suppression of Mn moments, but by the tendency of Cr appearing next to each other in the plane to form antiferromagnetic clusters. The results of these calculations are shown in note S2.

The bottom panel of Fig. 3B shows the coercive field, $\mu_0 H_c$, extracted from the magnetization measurement. The coercive field approximately follows the inverse of the zero-field magnetization, consistent with the flipping of the magnetization when the Zeeman energy $\mu_0 H_c M$ overcomes the domain depinning energy (*21*, *22*).

Near x^*, the coercive field exceeds 14 T, the maximum field achievable by the PPMS used. To our knowledge, this is the largest coercive field ever observed in a crystalline material (*23*). This massive coercivity is a result of the small magnetic moment observed combined with the large magnetocrystalline anisotropy of the Tb ions at low temperatures (*13*, *24*). These observations are consistent with $Tb(Mn_{1-x}Cr_x)_6Sn_6$ behaving as a nearly compensated ferrimagnet, exhibiting a giant coercive field at low temperatures between $0.30 \lesssim x \lesssim 0.45$, where the net Tb moments and the net Mn/Cr moments nearly cancel each other.

In contrast to magnetization, ρ_{AH} increases with Cr concentration. For samples very close to x^*, the hysteresis in ρ_{AH} cannot be detected by magnetic field sweep at base temperature simply because the coercive field exceeds 14 T. However, when the sample is field-cooled from high temperature, a large ρ_{AH} can still be observed even as M approaches zero (see fig. S12E in note S6). For $x > x^*$, the AHE switches sign, i.e., ρ_{AH} switches from positive to negative when the magnetization is positive. Given that the energy bands near the Fermi level are primarily composed of transition-metal d-orbitals, the sign change of the AHE is consistent with the AHE being driven by the transition-metal sites. In-depth analysis of the AHE will be presented in the "Enhancement of AHE with doping" section.

Temperature-induced magnetic compensation

In addition to chemical substitution, temperature is another effective parameter for controlling magnetic compensation. Figure 4A displays the previously shown out-of-plane magnetization as a function of temperature for a sample with $x = 0.49$. These data were collected as the sample is cooled under a 0.1-T c-axis magnetic field. At the spin reorientation transition temperature $T_{sr} = 150$ K, the magnetization abruptly increases as all moments reorient from in-plane to out-of-plane. Below T_{sr}, the magnetization reaches a maximum and then decreases with decreasing temperature. It crosses zero at $T^* = 114$ K and remains negative for temperatures below T^*.

To gain a deeper understanding of this behavior, we measured the field dependence of magnetization and Hall resistivity ρ_{xy} across a range of temperatures, as shown in the top and bottom rows of Fig. 4B, respectively. Each column represents data taken at the same temperature, which is noted above the column. In the 2.5 K data, in addition to the large hysteresis loop, a small additional paramagnetic contribution can be observed near $\mu_0 H = 0$ T in the magnetization versus field data. This contribution is highly sample dependent and only noticeable in samples with x greater than 0.4, suggesting that it may result from either disordered spins or a minor impurity phase. As the temperature increases, $\mu_0 H_c$ decreases substantially (the temperature

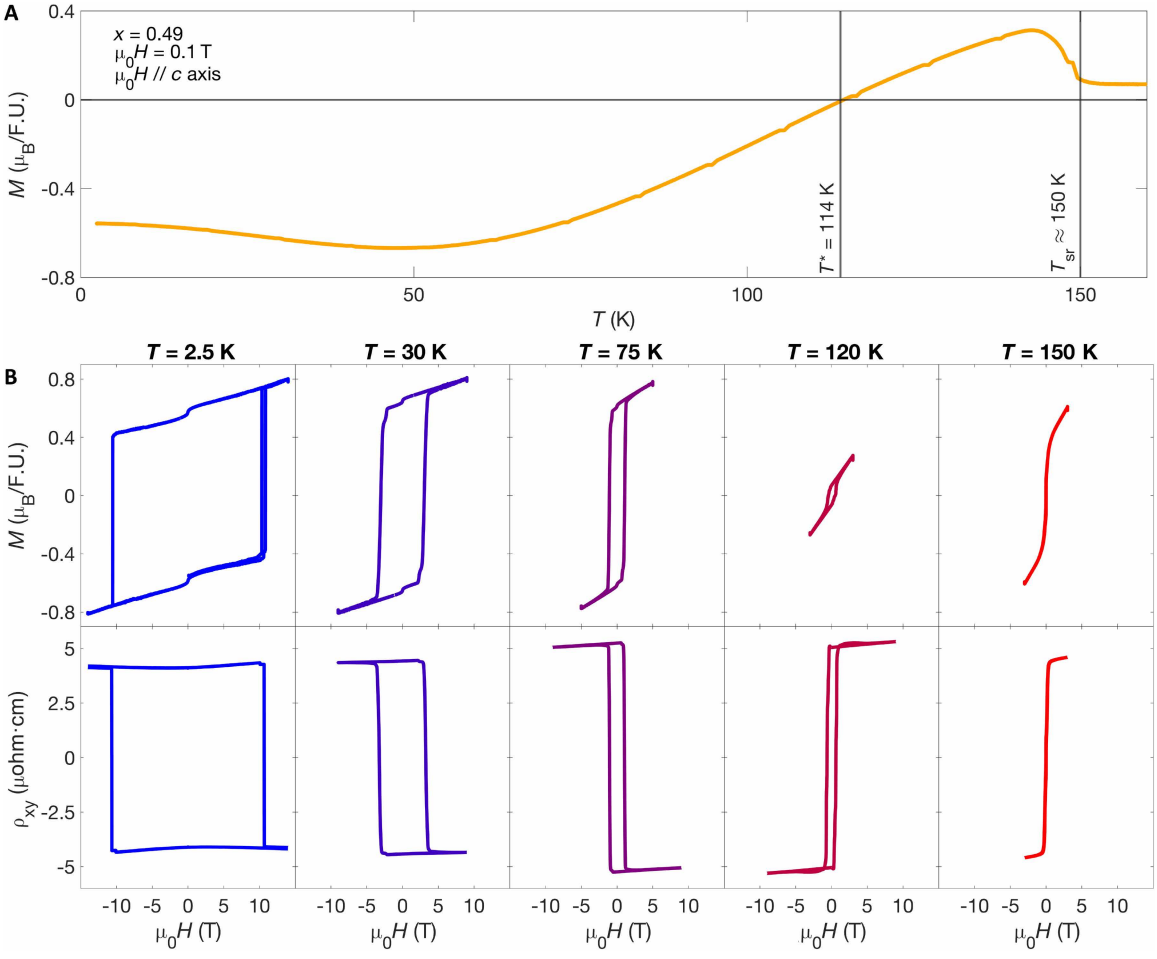

Fig. 4. Temperature dependence of magnetization and sign reversal of ρ_{AH}. (**A**) Low-field magnetization with an out-of-plane magnetic field for $x = 0.49$ as a function of temperature. (**B**) Magnetization (top row) and ρ_{xy} (bottom row) as a function of magnetic field at a variety of temperatures for the same sample. Plots in the same column are taken at the same temperature, which is indicated by the text on top of the column.

dependence of $\mu_0 H_c$ for multiple samples is detailed in note S3). Near T^* (≈120 K), the hysteresis loop in ρ_{xy} reverses direction, whereas the magnetization vanishes. As temperature increases above T^*, the magnetization increases again. The temperature dependence of the magnetization and the AHE mirrors the doping dependence at base temperature, indicating that the magnetic compensation can also be induced by temperature sweep. Instead of a reduction in average Mn/Cr moments due to Cr substitution, the magnetic compensation at T^* is driven by the reduction of the average Tb moments at elevated temperatures due to thermal fluctuations, which is the same mechanism that drives the spin reorientation transition (*13*). Such temperature-driven compensation is commonly seen in other rare-earth transition-metal alloy system, where sign switching of ρ_{AH} has been observed (*25*).

With these insights, we can now explain the magnetization reversal observed in the field-cooled measurements. In samples with $x >$ ≈0.4, the Mn/Cr moments have decreased sufficiently that the Tb moments can match them in magnitude at T^*. As the temperature continues to decrease in these samples, the net Tb moment becomes larger in magnitude than the Mn/Cr moment, causing the net magnetization to become anti-aligned with the external field. Additionally, the coercive field rapidly increases with decreasing temperature and exceeds the external field below T^*. Consequently, the magnetization becomes trapped in the reverse configuration, leading to an overall negative value of magnetization.

Enhancement of AHE with doping

We now turn to a more quantitative analysis of the AHE. Figure 5A and B shows the field dependence of Hall resistivity ρ_{xy} of samples with x = 0.28 and 0.43 measured at various temperatures. Similar plots of samples with other Cr concentrations can be found in note S4. All samples exhibit pronounced hysteresis and a well-defined AHE at zero field. For higher Cr concentrations, the AHE changes sign as a function of temperature as a result of magnetic compensation, as discussed in the previous section.

We calculated the anomalous Hall conductivity (AHC), σ_{AH}, using the relation $\sigma_{AH} = -\rho_{AH} / \left(\rho_{xx,0}^2 + \rho_{AH}^2\right)$, where $\rho_{xx,0}$ is the zero-field longitudinal resistivity. Figure 5C presents the AHC as a function of temperature for various Cr concentrations. To facilitate comparison across different samples without the influence of sign switching, we plot only the absolute value $|\sigma_{AH}|$. The results for $x = 0$ are consistent with previous reports (*13*). Cr doping does not substantially alter $|\sigma_{AH}|$, which changes by less than an order of magnitude across all measured Cr concentrations. Additionally, this quantity is not strongly dependent on temperature.

There are two contributions to the AHE: the intrinsic and extrinsic contributions. The former is originated from the Berry curvature of the band structure, while the latter is due to the skew scattering and side-jump mechanisms. Separating the intrinsic and extrinsic contributions of the AHE is a challenging task. Traditionally, this is done by fitting the AHC versus longitudinal conductivity to the function $\sigma_{AH} = a\sigma_{xx}^2 + c$, where $c = \sigma_{AH}^{int}$ is the intrinsic contribution, and the $a\sigma_{xx}^2$ term corresponds to extrinsic skew scattering and side-jump contributions (*26*). However, it has been shown that this function does not adequately fit the AHC in $TbMn_6Sn_6$. An additional nonstandard term, tentatively associated with spin fluctuations as discussed in (*13*), can be included to achieve a better fit, leading to an equation of the following form

$$\sigma_{AH} = a\sigma_{xx}^2 + c + d\sigma_{xx}^{-1} \quad (1)$$

We fitted the σ_{AH} versus σ_{xx} data for each sample, as shown in Fig. 6A and B for low and high doping levels, respectively, to extract σ_{AH}^{int} and σ_{AH}^{ext}. The dashed lines represent fits to the standard anomalous Hall equation, while the solid lines include an additional term proportional

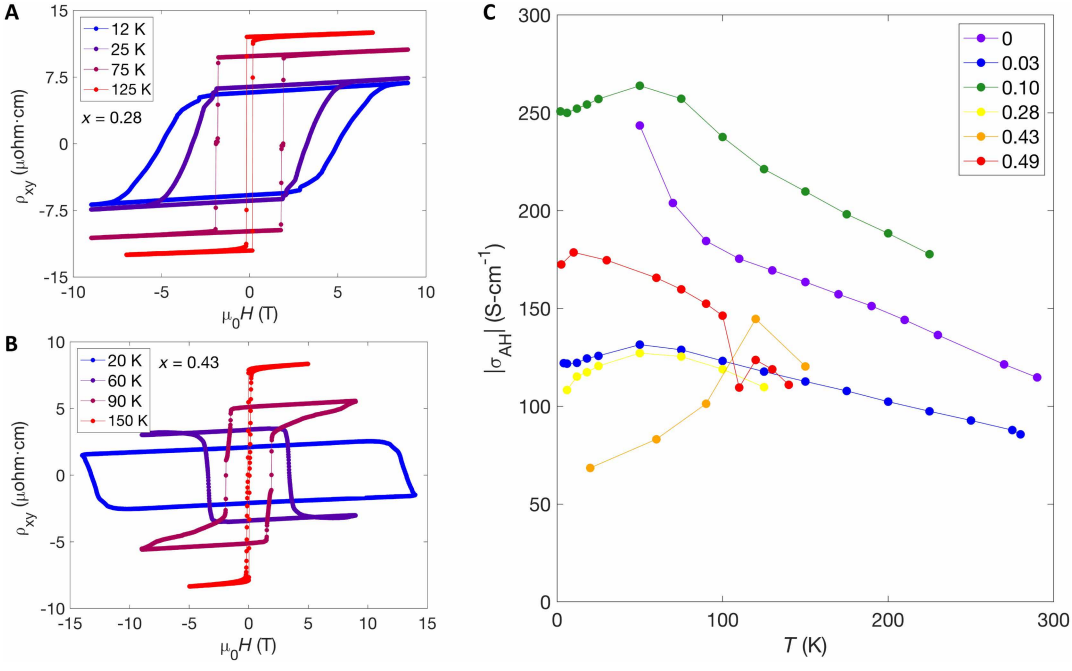

Fig. 5. AHE of $Tb(Mn_{1-x}Cr_x)_6Sn_6$. (**A** and **B**) ρ_{xy} as a function of $\mu_0 H$ at several temperatures for x = 0.28 and 0.43, respectively. (**C**) AHC $|\sigma_{AH}|$ as a function of temperature for a variety of dopings of $Tb(Mn_{1-x}Cr_x)_6Sn_6$.

to $\frac{1}{\sigma_{xx}}$ (Eq. 1). This additional term decisively improves the fit, especially for higher dopings.

The doping dependence of the fit parameters is presented in Table 1 and plotted in Fig. 7. It can be seen that the *a* coefficient associated with the skew scattering changes sign and increases dramatically as Cr concentration increases. This can be explained by the increase of disorder scattering due to Cr doping, and it is consistent with the substantial drop of residual resistance ratio (RRR), as shown in Fig. 7A. The extracted nonstandard parameter (*d*) increases roughly an order of magnitude over the measured dopings as shown in Fig. 7B, which is consistent with the enhanced Tb fluctuations corresponding to reduction of T_{sr} with increasing *x*. Also shown in this panel is a substantial enhancement of the extracted parameter *c* (= σ_{AH}^{int}) in orange. To further validate these fits, analyses using the resistivity form of the AHE equations are detailed in note S4 and yield similar results.

This extracted σ_{AH}^{int} with increasing *x* is plotted again in orange in Fig. 7C. Also shown is a simultaneous development of a large negative σ_{AH}^{ext} with increasing *x* (results shown for data taken at 50 K). Because of the opposite signs of the intrinsic and extrinsic contributions, the overall $|\sigma_{AH}^{total}|$ does not vary substantially with doping, and thus can be completely missed barring a proper scaling analysis.

DISCUSSION

$TbMn_6Sn_6$ has attracted appreciable attention due to reports of a large intrinsic AHE, initially attributed to quasi-2D gapped Dirac points, a characteristic feature of the kagome lattice band structure (*10*). However, this interpretation has been challenged by recent calculations, which suggest that the relevant Dirac points are far from the Fermi level and that the intrinsic AHE primarily arises from the anti-crossing of energy bands at other locations in momentum space (*12*, *13*, *21*). These studies further indicate that intrinsic AHC could be substantially enhanced if the material is hole-doped, a condition that can be achieved through Cr substitution.

The pronounced doping dependence of σ_{AH}^{int} observed in this work sheds more light on this debate. According to the gapped Dirac point model proposed in (*10*), σ_{AH}^{int} should decrease with Cr doping, as Cr doping lowers the Fermi level away from the gapped Dirac points, where the Berry curvature is concentrated. In contrast, the observed increase in σ_{AH}^{int} with Cr doping (i.e., hole doping) aligns better with scenarios proposed in (*13*, *12*, *21*). To verify this, we calculate σ_{AH}^{int} as a function of hole doping by rigid band shift of the Fermi level of $TbMn_6Sn_6$, as shown Fig. 7D. The good agreement between the experiment (orange curve in Fig. 7C) and the calculation (Fig. 7D) unambiguously confirms that multiple anti-crossing features in the band structure contribute to the intrinsic AHE.

In summary, we successfully grew Cr-doped single crystals of $TbMn_6Sn_6$ and studied their magnetic and magnetotransport properties. Cr doping tunes the ferrimagnetic state toward magnetic compensation with a giant coercive field. Additionally, with increased Cr doping, σ_{AH}^{int} becomes substantially larger, in strong agreement with first-principles calculations. This work offers a pathway for identifying and synthesizing compensated ferrimagnets with large intrinsic AHCs.

MATERIALS AND METHODS

Single crystals of $Tb(Mn_{1-x}Cr_x)_6Sn_6$ were synthesized utilizing a flux method similar to those previously reported for $TbMn_6Sn_6$

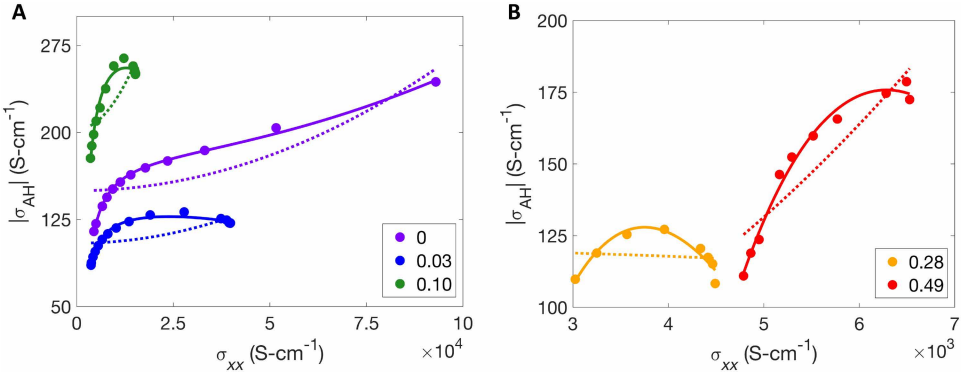

Fig. 6. Fitting of AHC. (**A** and **B**) $|\sigma_{AH}|$ as a function of σ_{xx} for low (A) and high (B) *x*. Dashed lines correspond to fits utilizing the standard anomalous Hall fitting function, and solid lines show fits that include the extra term described in the main text.

Table 1. Extracted parameters from conductivity fitting of AHE.

x	*a* (ohm·cm)	*c* ([ohm·cm]$^{-1}$)	*d* ([ohm·cm]$^{-2}$)
0	$(7.21 \pm 0.64) \times 10^{-9}$	186 ± 2.8	$(-3.26 \pm 0.22) \times 10^{5}$
0.03	$(-7.48 \pm 2.45) \times 10^{-9}$	140 ± 3.5	$(-2.04 \pm 0.18) \times 10^{5}$
0.10	$(-1.16 \pm 0.73) \times 10^{-7}$	313 ± 20.4	$(-4.87 \pm 0.88) \times 10^{5}$
0.28	$(-1.03 \pm 0.41) \times 10^{-5}$	562 ± 177	$(-1.08 \pm 0.43) \times 10^{6}$
0.49	$(-7.86 \pm 2.72) \times 10^{-6}$	1107 ± 262	$(-3.90 \pm 0.97) \times 10^{6}$

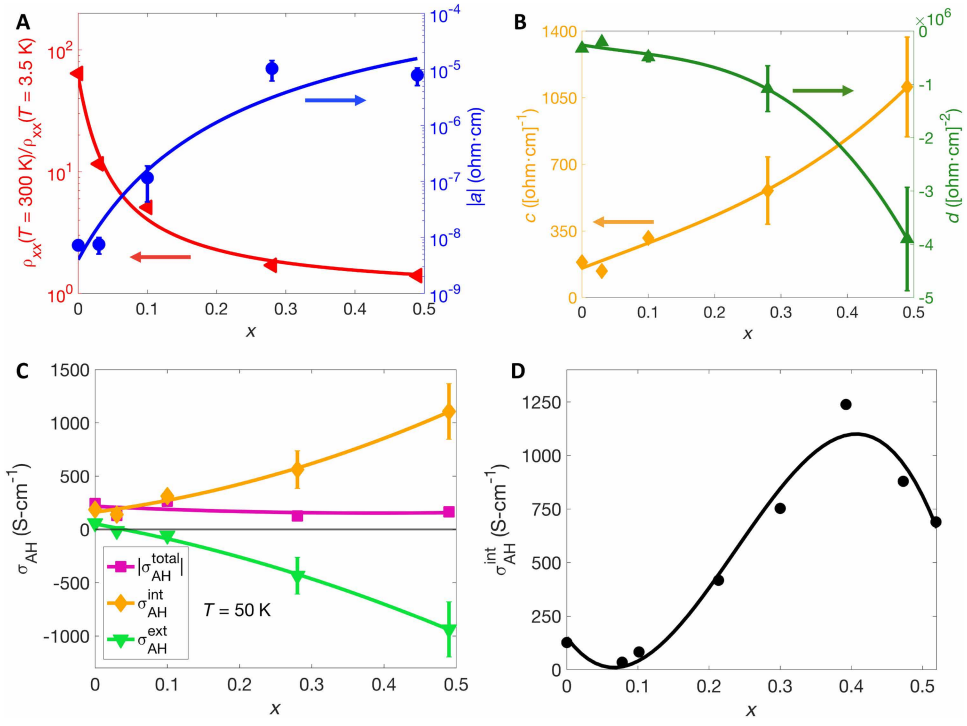

Fig. 7. Doping dependence of intrinsic and extrinsic AHE parameters. (**A**) Residual resistivity ratio and fit parameter *a* (extrinsic contribution) as a function of *x*. (**B**) Fit parameters *c* (intrinsic contribution) and *d* (spin fluctuation contribution) as a function of *x*. (**C**) $|\sigma_{AH}|$ and extracted σ_{AH}^{int} and σ_{AH}^{ext} at 50 K as a function of *x*. (**D**) Calculated σ_{AH}^{int} as a function of *x* using a rigid band model.

(*10*, *13*). Mixtures of Tb pieces (99.999%), Cr powder (99.99%), Mn powder (99.95%), and Sn shot (99.999%) were loaded into Canfield crucible sets (*27*) with atomic ratios Tb:(Cr, Mn):Sn 2.5:15:97.5 and then vacuum-sealed in quartz tubes. These were heated up to 1150°C in 12 hours, held at this temperature for 12 hours, and then cooled to 600°C in 150 hours. Then, the growths were decanted in a centrifuge to separate the excess flux from the crystals. The doping concentration x of each crystal of $Tb(Mn_{1-x}Cr_x)_6Sn_6$ used for measurements was determined using energy-dispersive x-ray spectroscopy (EDX) with a Sirion XL30 scanning electron microscope. Each crystal was polished before EDX measurements to remove residual flux on the surface of the crystal, and at least eight points on each crystal were measured. The measured spread in x_{EDX} for each crystal used in this study [and most of $Tb(Mn_{1-x}Cr_x)_6Sn_6$ in general] was limited to a few hundredths, indicating that the doping is reasonably homogeneous throughout the crystal. A plot of x_{EDX} as a function of x_{nom} (the nominal $\frac{Cr}{Cr+Mn}$ included in a growth) for a number of growths is presented in note S5 along with other EDX information. Throughout this paper, the measured x_{EDX} is referred to as x for simplicity. Using the growth technique outlined here, crystals of $Tb(Mn_{1-x}Cr_x)_6Sn_6$ with $0 < x < 0.55$ were able to be grown. Some crystals with $x \gtrsim 0.3$ had Sn inclusions that could be detected via transport measurements (shorting of the resistivity below Sn's superconducting transition) and/or seen under a microscope. Measurements performed on these samples are not reported. It should be noted that for relatively high x_{nom} ($\geq$0.5), secondary phases of Cr (cubic crystals) and Tb_3Sn_7 (plate-like crystals) were also found in the growths, and growths with $x_{nom} > 0.6$ did not provide any crystals.

Transport measurements were performed on samples that were polished and cut by a wire saw to be bars with dimensions roughly 1 mm by 0.4 mm by 0.05 mm. Silver paste and gold wires were used to make five point (Hall pattern) contacts. These measurements were performed in a Quantum Design Dynacool PPMS with standard lock-in techniques in temperatures ranging from 1.7 to 400 K and in magnetic fields up to 14 T. To eliminate any contributions from contact misalignment, the in-line and Hall resistivities were symmetrized and anti-symmetrized with magnetic field, respectively.

Magnetization measurements were performed with the vibrating sample magnetometer option of the PPMS. Samples of the same size as the transport samples were attached to a quartz paddle with GE varnish such that the magnetic field was either out-of-plane (i.e., parallel to the *c* axis) or in-plane.

Electron microscopy imaging and spectroscopy were carried out by an aberration-corrected STEM in a Nion UltraSTEM 100 (*28*). The electron microscope was operated with an acceleration voltage of 100 kV, using a semi-convergence angle of 32 mrad. High-angle annular dark field (HAADF) images, also known as *Z*-contrast images due to the intensity being proportional to atomic number, were acquired with an inner (outer) semi-angle of 80 (200) mrad. EELS data were acquired with a collection semi-angle of 48 mrad.

The DFT calculations were performed using a full-potential linear augmented plane wave (FP-LAPW) method, as implemented in wien2k (*29*, *30*). Spin-orbit coupling (SOC) was included using a second variational method. The generalized gradient approximation by Perdew, Burke, and Ernzerhof (PBE) (*31*) was used for the exchange-correlation potentials. To generate the self-consistent potential and charge, we used $R_{MT} \cdot K_{max} = 8.0$ with Muffin-tin (MT) radii $R_{MT} =$

2.8, 2.4, 2.4, and 2.5 atomic units (a.u.) for Tb, Mn, Cr, and Sn, respectively. The calculations are performed with 4800 k-points in the full Brillouin zone (FBZ) and iterated until the charge differences between consecutive iterations are smaller than $10^{-4}e$ and the total energy differences are lower than 10^{-2} mRy/cell. The strongly correlated Tb-4f electrons are treated using the DFT + U (U = 10 eV) method with the fully localized limit (FLL) double-counting scheme (*32*). $TbMn_6Sn_6$ consists of six equivalent Mn atoms, which are replaced by one, two, or three Cr atoms depending on the doping concentration. We constructed one, three, and three configurations by replacing on one, two, and three Mn atoms to Cr atoms, respectively, and compared magnetic moments and total energies of each configuration. We also performed virtual crystal (VC) calculations to confirm if the rigid band model is reliable in this study. We kept lattice parameters the same as that of $TbMn_6Sn_6$ since the lattice parameter change is less than 0.5% up to 33% doping (*18*).

A realistic tight-binding (TB) Hamiltonian was constructed using the maximally localized Wannier functions (MLWFs) method (*33*–*35*) implemented in Wannier90 (*36*) after the self-consistent DFT calculations were performed using Wien2k. To circumvent complications associated with the 4*f* state of the Tb atom while preserving the main physics, we used an open-core method for the 4*f* state. A set of 118 Wannier functions (WFs) consisting of Tb-5d, Mn-3d, and Sn-s,p orbitals offers an effective representation of the electronic structure near the Fermi level (E_F). The intrinsic AHC can be calculated by integrating the Berry curvature over the BZ (*37*)

$$\sigma_{\alpha\beta} = -\frac{e^2}{\hbar}\int_{BZ}\frac{d\vec{k}}{(2\pi)^3}\sum_n f\left(E_{\vec{nk}}\right)\Omega_{n,\alpha\beta}\left(\vec{k}\right) \quad (2)$$

where $f\left(E_{\vec{nk}}\right)$ is the Fermi-Dirac distribution, $\Omega_{n,\alpha\beta}\left(\vec{k}\right)$ is the contribution to the Berry curvature from state n, and $\alpha, \beta = \{x, y, z\}$. We implemented Eq. 2 within an in-house ab initio TB framework (*38*). A dense 256^3 k-point mesh is used for the AHC calculations in TB to ensure good convergence.

Supplementary Materials

This PDF file includes:

Notes S1 to S6
Figs. S1 to S12
Tables S1 to S6
References

REFERENCES AND NOTES

1. J. Finley, L. Liu, Spintronics with compensated ferrimagnets. *Appl. Phys. Lett.* **116**, 110501 (2020).
2. S. K. Kim, G. S. D. Beach, K.-J. Lee, T. Ono, T. Rasing, H. Yang, Ferrimagnetic spintronics. *Nat. Mater.* **21**, 24–34 (2022).
3. H.-A. Zhou, T. Xu, H. Bai, W. Jiang, Efficient spintronics with fully compensated ferrimagnets. *J. Physical Soc. Japan* **90**, 081006 (2021).
4. I. Mazin, Editorial: Altermagnetism—A new punch line of fundamental magnetism. *Phys. Rev. X* **12**, 040002 (2022).
5. P. Hansen, C. Clausen, G. Much, M. Rosenkranz, K. Witter, Magnetic and magneto-optical properties of rare-Earth transition-metal alloys containing Gd, Tb, Fe, Co. *J. Appl. Phys.* **66**, 756–767 (1989).
6. T. Fujita, M. B. A. Jalil, S. G. Tan, S. Murakami, Gauge fields in spintronics. *J. Appl. Phys. 110*, 121301 (2011).
7. M. Li, Q. Wang, G. Wang, Z. Yuan, W. Song, R. Lou, Z. Liu, Y. Huang, Z. Liu, H. Lei, Z. Yin, S. Wang, Dirac cone, flat band and saddle point in kagome magnet YMn_6Sn_6. *Nat. Commun.* **12**, 3129 (2021).
8. S. Peng, Y. Han, G. Pokharel, J. Shen, Z. Li, M. Hashimoto, D. Lu, B. R. Ortiz, Y. Luo, H. Li, M. Guo, B. Wang, S. Cui, Z. Sun, Z. Qiao, S. D. Wilson, J. He, Realizing Kagome band structure in two-dimensional kagome surface states of RV_6Sn_6(R = Gd, Ho). *Phys. Rev. Lett.* **127**, 266401 (2021).
9. Y. Hu, X. Wu, Y. Yang, S. Gao, N. C. Plumb, A. P. Schnyder, W. Xie, J. Ma, M. Shi, Tunable topological Dirac surface states and van Hove singularities in kagome metal GdV_6Sn_6. *Sci. Adv.* **8**, eadd2024 (2022).
10. J.-X. Yin, W. Ma, T. A. Cochran, X. Xu, S. S. Zhang, H.-J. Tien, N. Shumiya, G. Cheng, K. Jiang, B. Lian, Z. Song, G. Chang, I. Belopolski, D. Multer, M. Litskevich, Z. J. Cheng, X. P. Yang, B. Swidler, H. Zhou, H. Lin, T. Neupert, Z. Wang, N. Yao, T. R. Chang, S. Jia, M. Zahid Hasan, Quantum-limit Chern topological magnetism in $TbMn_6Sn_6$. *Nature* **583**, 533–536 (2020).
11. H. Zhang, J. Koo, C. Xu, M. Sretenovic, B. Yan, X. Ke, Exchange-biased topological transverse thermoelectric effects in a Kagome ferrimagnet. *Nat. Commun.* **13**, 1091 (2022).
12. Y. Lee, R. Skomski, X. Wang, P. P. Orth, Y. Ren, B. Kang, A. K. Pathak, A. Kutepov, B. N. Harmon, R. J. McQueeney, I. I. Mazin, L. Ke, Interplay between magnetism and band topology in the kagome magnets RMn_6Sn_6. *Phys. Rev. B* **108**, 045132 (2023).
13. D. C. Jones, S. Das, H. Bhandari, X. Liu, P. Siegfried, M. P. Ghimire, S. S. Tsirkin, I. I. Mazin, N. J. Ghimire, Origin of spin reorientation and intrinsic anomalous Hall effect in the kagome ferrimagnet $TbMn_6Sn_6$. *Phys. Rev. B* **110**, 115134 (2024).
14. H. Bhandari, Z. Ning, P.-H. Chang, P. E. Siegfried, R. B. Regmi, Mohamed El. Gazzah, A. V. Davydov, A. G. Oliver, L. Ke, I. I. Mazin, N. J. Ghimire, Three-dimensional nature of anomalous Hall conductivity in YMn_6Sn_6-xGax, x ~ 0.55. arXiv:2411.12134 [cond-mat. mtrl-sci] (2024).
15. B. C. El Idrissi, G. Venturini, B. Malaman, D. Fruchart, Magnetic structures of $TbMn_6Sn_6$ and $HoMn_6Sn_6$ compounds from neutron diffraction study. *J. Less Common Metals* **175**, 143–154 (1991).
16. D. M. Clatterbuck, K. A. Gschneidner, Magnetic properties of RMn_6Sn_6 (R = Tb, Ho, Er, Tm, Lu) single crystals. *J. Magn. Magn. Mater.* **207**, 78–94 (1999).
17. S. X. M. Riberolles, T. J. Slade, R. L. Dally, P. M. Sarte, B. Li, T. Han, H. Lane, C. Stock, H. Bhandari, N. J. Ghimire, D. L. Abernathy, P. C. Canfield, J. W. Lynn, B. G. Ueland, R. J. McQueeney, Orbital character of the spin-reorientation transition in $TbMn_6Sn_6$. *Nat. Commun.* **14**, 2658 (2023).
18. P. Schobinger-Papamantellos, G. André, J. Rodriguez-Carvajal, H. Duijn, K. Buschow, Magnetic ordering in $TbMn_{6-x}CrxSn_6$ (x = 1, 2) compounds studied by neutron diffraction and magnetic measurements. *J. Alloys Compd.* **306**, 47–55 (2000).
19. I. Fita, R. Puzniak, A. Wisniewski, V. Markovich, Spin switching and unusual exchange bias in the single-crystalline $GdCrO_3$ compensated ferrimagnet. *Phys. Rev. B* **100**, 144426 (2019).
20. P. Schobinger-Papamantellos, J. Rodríguez-Carvajal, K. H. J. Buschow, Atomic disorder and canted ferrimagnetism in the $TbCr_6Ge_6$ compound. A neutron study. *J. Alloys Compd.* **255**, 67–73 (1997).
21. A. K. Nayak, M. Nicklas, S. Chadov, P. Khuntia, C. Shekhar, A. Kalache, M. Baenitz, Y. Skourski, V. K. Guduru, A. Puri, U. Zeitler, J. M. D. Coey, C. Felser, Design of compensated ferrimagnetic Heusler alloys for giant tunable exchange bias. *Nat. Mater.* **14**, 679–684 (2015).
22. L. Zhu, L. Zhu, Q. Liu, X. Lin, Giant coercivity, resistivity upturn, and anomalous Hall effect in ferrimagnetic FeTb. *Phys. Rev. B* **108**, 014420 (2023).
23. E. A. Gorbachev, E. S. Kozlyakova, L. A. Trusov, A. E. Sleptsova, M. A. Zykin, P. E. Kazin, Design of modern magnetic materials with giant coercivity. *Russ. Chem. Rev.* **90**, 1287–1329 (2021).
24. E. Rosenberg, J. M. DeStefano, Y. Guo, J. S. Oh, M. Hashimoto, D. Lu, R. J. Birgeneau, Y. Lee, L. Ke, M. Yi, J. H. Chu, Uniaxial ferromagnetism in the kagome metal TbV_6Sn_6. *Phys. Rev. B* **106**, 115139 (2022).
25. T. R. McGuire, R. J. Gambino, R. C. Taylor, Hall effect in amorphous thin-film magnetic alloys. *J. Appl. Phys.* **48**, 2965–2970 (1977).
26. Y. Tian, L. Ye, X. Jin, Proper scaling of the anomalous Hall effect. *Phys. Rev. Lett.* **103**, 087206 (2009).
27. P. C. Canfield, T. Kong, U. S. Kaluarachchi, N. H. Jo, Use of frit-disc crucibles for routine and exploratory solution growth of single crystalline samples. *Philos. Mag.* **96**, 84–92 (2016).
28. O. Krivanek, G. Corbin, N. Dellby, B. Elston, R. Keyse, M. Murfitt, C. Own, Z. Szilagyi, J. Woodruff, An electron microscope for the aberration-corrected era. *Ultramicroscopy* **108**, 179–195 (2008).
29. P. Blaha, K. Schwarz, G. Madsen, D. Kvasnicka, J. Luitz, *Wien2k: An Augmented Plane Wave Plus Local Orbitals Program for Calculating Crystal Properties* (Technische Universität Wien, 2001).
30. P. Blaha, K. Schwarz, F. Tran, R. Laskowski, G. K. H. Madsen, L. D. Marks, WIEN2k: An APW+lo program for calculating the properties of solids. *J. Chem. Phys.* **152**, 074101 (2020).
31. J. P. Perdew, K. Burke, M. Ernzerhof, Generalized gradient approximation made simple. *Phys. Rev. Lett.* **77**, 3865–3868 (1996).

32. V. I. Anisimov, I. V. Solovyev, M. A. Korotin, M. T. Czyżyk, G. A. Sawatzky, Density-functional theory and NiO photoemission spectra. *Phys. Rev. B* **48**, 16929–16934 (1993).
33. N. Marzari, D. Vanderbilt, Maximally localized generalized Wannier functions for composite energy bands. *Phys. Rev. B* **56**, 12847–12865 (1997).
34. I. Souza, N. Marzari, D. Vanderbilt, Maximally localized Wannier functions for entangled energy bands. *Phys. Rev. B* **65**, 035109 (2001).
35. N. Marzari, A. A. Mostofi, J. R. Yates, I. Souza, D. Vanderbilt, Maximally localized Wannier functions: Theory and applications. *Rev. Mod. Phys.* **84**, 1419–1475 (2012).
36. A. A. Mostofi, J. R. Yates, G. Pizzi, Y.-S. Lee, I. Souza, D. Vanderbilt, N. Marzari, An updated version of wannier90: A tool for obtaining maximally-localised Wannier functions. *Comput. Phys. Commun.* **185**, 2309–2310 (2014).
37. X. Wang, J. R. Yates, I. Souza, D. Vanderbilt, Ab initiocalculation of the anomalous Hall conductivity by Wannier interpolation. *Phys. Rev. B* **74**, 195118 (2006).
38. L. Ke, Intersublattice magnetocrystalline anisotropy using a realistic tight-binding method based on maximally localized Wannier functions. *Phys. Rev. B* **99**, 054418 (2019).
39. K. Momma, F. Izumi, *VESTA* 3 for three-dimensional visualization of crystal, volumetric and morphology data. *J. Appl. Cryst.* **44**, 1272–1276 (2011).
40. S. X. M. Riberolles, T. J. Slade, D. L. Abernathy, G. E. Granroth, B. Li, Y. Lee, P. C. Canfield, B. G. Ueland, L. Ke, R. J. McQueeney, Low-temperature competing magnetic energy scales in the topological ferrimagnet $TbMn_6Sn_6$. *Phys. Rev. X* **12**, 021043 (2022).
41. S. Demirtas, A. R. Koymen, Coercivity and exchange bias near the compensation temperature for inhomogeneous Fe/Gd ferrimagnets. *J. Appl. Phys.* **95**, 4949–4952 (2004).
42. C. Fowley, K. Rode, Y.-C. Lau, N. Thiyagarajah, D. Betto, K. Borisov, G. Atcheson, E. Kampert, Z. Wang, Y. Yuan, S. Zhou, J. Lindner, P. Stamenov, J. M. D. Coey, A. M. Deac, Magnetocrystalline anisotropy and exchange probed by high-field anomalous Hall effect in fully compensated half-metallicMn2RuxGathin films. *Phys. Rev. B* **98**, 220406 (2018).
43. S. Onoda, N. Sugimoto, N. Nagaosa, Quantum transport theory of anomalous electric, thermoelectric, and thermal Hall effects in ferromagnets. *Phys. Rev. B* **77**, 165103 (2008).
44. R. J. Pérez, B. Sundman, Thermodynamic assessment of the Cr-Sn binary system. *Calphad* **25**, 59–66 (2001).
45. M. Aljarrah, S. Obeidat, R. H. Fouad, M. Rababah, A. Almagableh, A. Itradat, I. E. T. Science, Thermodynamic calculations of the Mn–Sn, Mn–Sr and Mg–Mn–{Sn, Sr} systems. *IET Sci. Meas. Technol.* **9**, 681–692 (2015).

Acknowledgments

Funding: This work is mainly supported by the Air Force Office of Scientific Research under grant FA9550-21-1-0068, the David and Lucile Packard Foundation, and the Gordon and Betty Moore Foundation's EPiQS Initiative, grant no. GBMF6759 to J.-H.C. This material is based upon work supported by the National Science Foundation Graduate Research Fellowship Program under grant no. DGE-2140004. Any opinions, findings, and conclusions or recommendations expressed in this material are those of the authors and do not necessarily reflect the views of the National Science Foundation. O.P. acknowledges support from the University of Washington Mary Gates Research Scholarship. The TEM work was supported by NSF through the University of Washington Molecular Engineering Materials Center, a Materials Research Science and Engineering Center (DMR-2308979). The material synthesis was partially supported by NSF Partnerships for Research and Education in Materials (PREM) grant DMR-2121953. Part of this work was conducted at the Molecular Analysis Facility, a National Nanotechnology Coordinated Infrastructure site at the University of Washington, which is supported in part by the National Science Foundation (grant NNCI-1542101), the University of Washington, the Molecular Engineering & Sciences Institute, the Clean Energy Institute, and the National Institutes of Health. STEM imaging was conducted as part of a user project at the Center for Nanophase Materials Sciences (CNMS), which is a US DOE, Office of Science User Facility at Oak Ridge National Laboratory. Crystal structure images were generated with VESTA (*39*). The theory work was supported by the U.S. Department of Energy, Office of Science, Office of Basic Energy Sciences, Materials Sciences and Engineering Division. The software implementation was supported by the USDOE Early Career Research Program. Ames Laboratory is operated for the U.S. Department of Energy by Iowa State University under contract no. DE-AC02-07CH11358. I.I.M. acknowledges support from the National Science Foundation under award no. DMR-2403804. **Author contributions:** J.M.D., E.R., O.P., and K.H. grew the samples and performed the magnetization and magnetotransport measurements. G.R. performed the STEM experiments and analyzed the data with guidance from J.C.I. Y.L., Z.N., L.K., and I.I.M. performed DFT calculations and contributed to the theoretical analysis. J.-H.C. oversaw the project. J.M.D., E.R., and J.-H.C. wrote the manuscript with input from all authors. **Competing interests:** The authors declare that they have no competing interests. **Data and materials availability:** All data needed to evaluate the conclusions in the paper are present in the paper and/or the Supplementary Materials. The data for the plots in the main paper can be found at https://zenodo.org/records/15677103.

Submitted 24 March 2025
Accepted 31 July 2025
Published 29 August 2025
10.1126/sciadv.adx4671